iScience

CellPress
OPEN ACCESS

Article

3D-Microbattery Architectural Design Optimization Using Automatic Geometry Generator and Transmission-Line Model

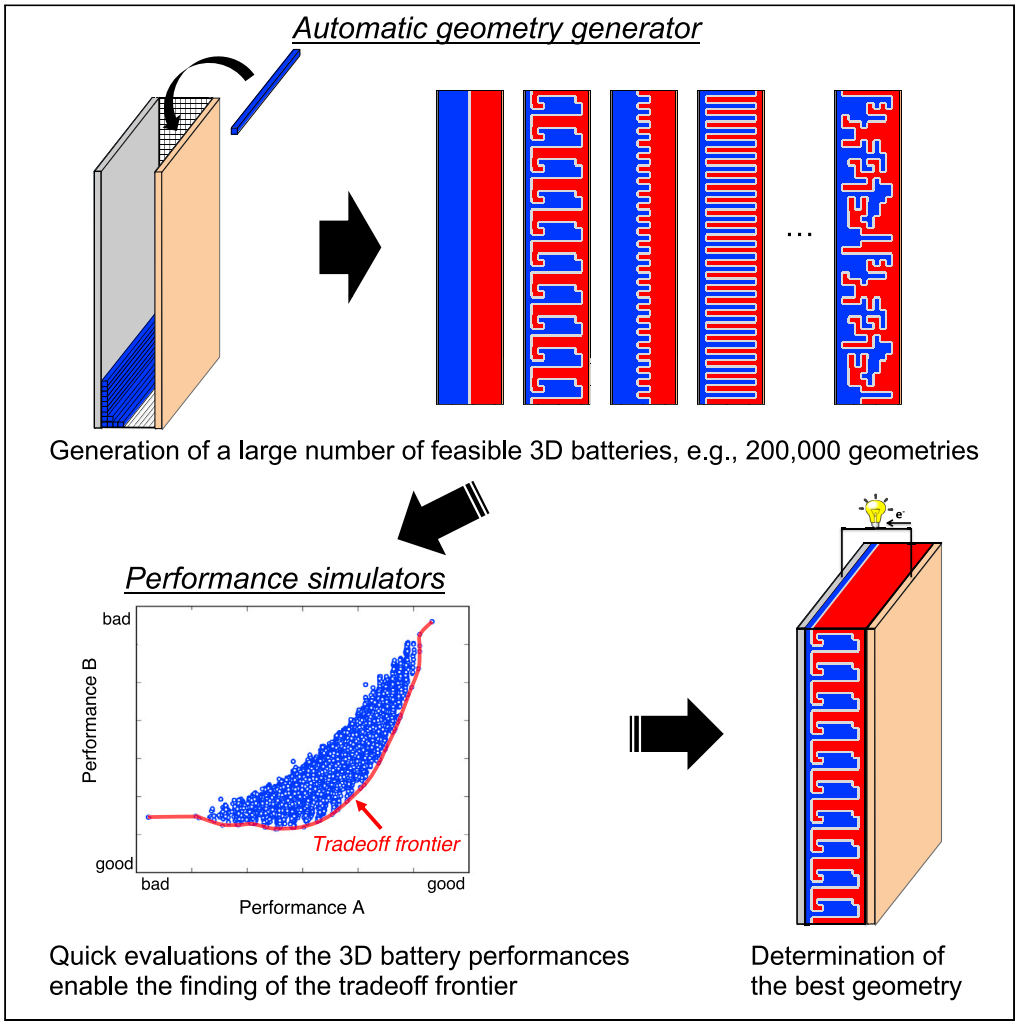

Kaito Miyamoto, Tsuyoshi Sasaki, Tomoki Nishi, Yuichi Itou, Kensuke Takechi

kaito.miyamoto@toyota.com

HIGHLIGHTS

The automatic geometry generator created feasible 3D microbattery architectures

The use of TLM enabled quick evaluation of the internal resistance of the 3D battery

The optimization system could evaluate the performance of 200,000 3D microbatteries

The optimized battery showed better performance over the interdigitated geometry

Miyamoto et al., iScience *23*, 101317
July 24, 2020
https://doi.org/10.1016/j.isci.2020.101317

iScience

CellPress
OPEN ACCESS

Article

3D-Microbattery Architectural Design Optimization Using Automatic Geometry Generator and Transmission-Line Model

Kaito Miyamoto,[1,2,3,*] Tsuyoshi Sasaki,[2] Tomoki Nishi,[2] Yuichi Itou,[2] and Kensuke Takechi[2]

SUMMARY

Optimization of the 3D battery architecture is crucial to improve the performance of microbatteries. However, such optimization is difficult and time consuming by hand for even experts. In this article, we propose a battery optimization system, which consists of an automatic geometry generator and performance simulators. The geometry generator creates feasible 3D batteries without using any human intuition and experience for the spatial arrangement of positive and negative electrodes. For quick evaluation of the internal resistance, which relates power and energy densities, we propose the transmission line model, the so-called 3D porous electrode model, as one of the performance simulators. To show the effectiveness of the optimization system, we designed the lithium-ion microbatteries. In the trade-off frontier for the internal resistance and the capacity, we successfully found a new battery architecture that has higher power and energy densities over the conventional interdigitated plates configuration.

INTRODUCTION

The rapid development of information technology since the end of the twentieth century and the technological progress of sensors and devices have familiarized the concept of the Internet of Things (IoT). In particular, the development of high-speed and large-capacity communication infrastructure on a global basis, drastic reductions in sensor unit prices, and the advent of smart devices such as smartphones and tablet computers have led to the explosive spread of IoT services since 2010. The number of internet-connected devices surpassed the number of internet users in 2008 (Swan, 2012), and, at present, further spread of IoT in various fields, including medical care, automotive and transportation, and agriculture, is expected (Markit, 2017).

So far, the miniaturization of the sensors and devices has significantly contributed to the rapid growth of the IoT ecosystem. However, compared with such technological progress on the sensors and devices, the miniaturization technology of the power sources for the off-grid operation of the electronics has not been well established, which hinders further prevalence of the IoT (Swan, 2012; Hur et al., 2018). Especially, for the integration with microelectronics, the high areal energy density is recognized as one of the key properties for such power sources (Long et al., 2004; Zhang et al., 2017; Zhu et al., 2017; Wei et al., 2017).

The lithium-ion batteries, due to their exceptional performance represented by high energy density, high operating voltage, as well as long lifetime, have been used as the power sources in a variety of fields, such as electronics, e.g., smartphones and laptop computers, and electric and hybrid vehicles, and their miniature batteries, the so-called lithium-ion microbatteries, have been considered to be one of the promising candidates for the IoT-enabled power sources. Indeed, thin-film microbatteries were already commercialized, and their applications to the IoT devices, such as sensors, renewable energy storage devices, RFID (radio-frequency identification) tags, and smart cards, have been explored (Dudney, 2008). However, the thin-film microbatteries have a problem with their low areal energy densities (1 mWh/cm^2) (Pikul and Ning, 2018). Although the use of thicker electrodes improves the areal energy density, it leads to lower power density due to the increase of the internal resistance.

To improve the areal energy density while maintaining high power density, the three-dimensional design of the microbattery at the full cell level has attracted attention (Long et al., 2004). One example of such 3D

[1]Toyota Research Institute of North America, Toyota Motor North America, Inc., 1555, Woodridge Avenue, Ann Arbor, MI 48105, USA

[2]Toyota Central R&D Labs., Inc., 41-1, Yokomichi, Nagakute, Aichi 480-1192, Japan

[3]Lead Contact

*Correspondence: kaito.miyamoto@toyota.com

https://doi.org/10.1016/j.isci.2020.101317

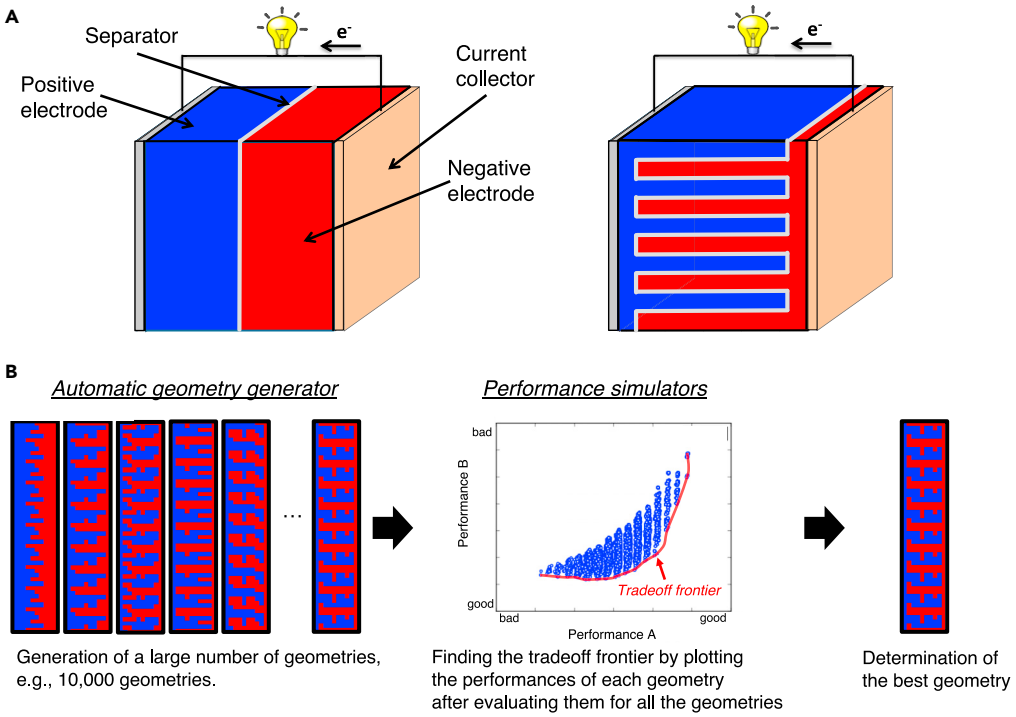

Figure 1. Examples of 3D Battery Geometries and the Battery Optimization System

(A) Comparison of conventional battery (left) and one example of the 3D designed batteries (right: interdigitated anode and cathode plates configuration).

(B) The framework of the battery optimization system. For simplicity, the current collectors and separator are removed from the battery geometries.

batteries is shown in Figure 1A. The benefit of the geometrical modification is the lowering of the internal resistance by changing the ion and electron transport distances without reducing the battery capacity. The recent advancement of a variety of 3D manufacturing technologies (Sun et al., 2013; Wei et al., 2017; Hur et al., 2018) has allowed the realization of the 3D microbattery (Ning et al., 2015; Mazor et al., 2012; Pikul et al., 2013; Sun et al., 2013; Fu et al., 2016; Izumi et al., 2012; Hur et al., 2018). For example, Ning et al. fabricated the on-chip high-energy-density 3D lithium-ion microbatteries by combining 3D holographic lithography and conventional photolithography (Ning et al., 2015). Using template-assisted electrodeposition, Pikul et al. achieved the high-power lithium-ion microbatteries where nanoporous electrodes were used as the electrodes in the 3D interdigitated battery (Pikul et al., 2013). Very recently, Hur et al. proposed the full 3D battery fabrication process based on semiconductor processing technologies, and their battery showed excellent performance, e.g., more than two times higher discharge capacities (up to 1.8 mAh cm^{-2}) compared with the highest thin-film batteries and attainment of 100 cycles (Hur et al., 2018).

Although such drastic improvements of a variety of the fabrication processes realized the 3D microbatteries having both high power and energy densities, the electrode structures are limited to simple geometries such as interdigitated plate (Sun et al., 2013; Pikul et al., 2013; Fu et al., 2016; Izumi et al., 2012) or cylindrical (Hur et al., 2018) electrodes, and, therefore, the battery performance is restricted by such electrode structures. To design the 3D battery architecture beyond the interdigitated configurations, the 3D battery optimization method at the full cell level is vital. Also, the 3D battery optimization method is crucial from the point of view of industrial demand because there are a variety of IoT devices that have different functions, and it is demanding to optimize the battery following the requirements of each IoT device by hand. However, there are no reports regarding the 3D battery optimization methods at the full cell level.

In this article, we propose a novel battery optimization system at the full cell level, which consists of an automatic geometry generator and performance simulators (Figure 1B). So far, battery optimizations have been carried out using continuum simulations (McKelvey et al., 2020). However, most of such methods investigate only the influence of simple structural change (such as width, length, pitch, and end shape) of the

interdigitated electrodes to the battery performance (Hart et al., 2003; McKelvey et al., 2017; Zadin et al., 2010, 2011; Zadin and Brandell, 2011; Priimägi et al., 2016; Miranda et al., 2016; Pikul et al., 2017; Li et al., 2018). Although Zadin et al. optimized the 3D electrode geometry using the level-set method and obtained the complicated-shaped electrodes, the design space was too simple as the practical battery cell (one tooth per electrode) (Zadin et al., 2013). In addition, all the previous works start optimizations from the interdigitated configurations. Contrary to this, our geometry generator designs the full cell based on random sampling, without using any human intuition and experience for the spatial arrangement of positive and negative electrodes, by only receiving the size and resolution of the 3D battery cell and the volume ratio of the positive and negative electrodes as the input data. For compatibility with the geometry generator, as one of the performance simulators, we newly propose the transmission line model, the so-called 3D porous electrode model, to compute the internal resistance of the 3D battery quickly. As shown in Figure 1B, our optimization system designs the 3D battery by generating a large number of battery geometries, evaluating battery performances of each geometry quickly, and, then, creating the trade-off frontier (a set of data points that are not dominated by other data points in a given dataset). We show the effectiveness of our method by creating the trade-off frontier for the internal resistance and capacity that relate to the power and energy densities of the 3D battery and finding the new battery geometry that has higher power and energy densities over the interdigitated plates configuration.

RESULTS AND DISCUSSION

Automatic Geometry Generator

We generate the battery cell using the newly proposed randomized algorithm. In this article, for simplicity, we generate the 3D battery having two degrees of freedom for electrode designs, e.g., the interdigitated anode and cathode plates configuration shown in Figure 1A and geometries illustrated in Figure 1B. However, we should emphasize that it is straightforward to extend our algorithm to the 3D electrode designs such as the full cell shown in Hur et al. (2018). Also, we assume that the current collectors are placed as shown in Figure 1A, i.e., the current collector plate for the positive electrode is located in the left-hand side of the cell and that for the negative electrode in the right-hand side. Here, we call the mixture of active material, a polymer binder, and an electrolyte filling the pores as the positive and negative electrodes because we assume porous electrodes. When necessary, the conductive agents also become components of the electrode.

The central idea of the battery generation method is illustrated in Figure 2A. At first, the vacant cell with predefined width (W), height (H), and depth (D) is prepared and the space is divided into finite elements. Then, the space is filled in with the cuboid-shaped electrodes one by one after determining the numbers of the (cuboid-shaped) positive and negative electrodes using the volume ratio of the positive and negative electrodes (which is specified in the input). In this article, we call the cuboid-shaped electrode as an electrode element. Here, it is noteworthy that we need to determine only the locations of positive and negative electrode elements, i.e., the position of the separator is automatically determined once the positions of all electrode elements were determined. The fineness of the finite element mesh may be determined by following the resolution of fabrication methods such as the 3D printers.

In our code, the battery geometry and the spatial positions of the positive and negative electrodes are represented as a matrix and its elements, respectively. For example, the interdigitated geometry shown in Figure 2A is represented by Figure 2B, where "1" and "3" represent the positive and negative electrode elements, respectively. We call this matrix as the geometry matrix. Also, the vacant cell is represented by a zero matrix. Thus, the geometry generation process shown in Figure 2A corresponds to the one-by-one determination of each element value ("1" or "3") in the matrix from the zero matrix. The actual 3D battery can be constructed from the geometry matrix and the information about the cell size (W, H, and D).

Each geometry-matrix-element value is determined randomly. However, if the geometry matrix is created by simply filling in with "1" or "3" randomly without any restrictions, a huge number of unacceptable geometries are generated, as exemplified in Figure 2C. The geometry in the figure has two kinds of clear problems as a battery: "the negative/positive electrode comes next to the current collector for the positive/negative electrode (the short circuit problem)" and "isolation or surrounding of the positive/negative electrode (the isolation problem)." One of the key points of our randomized algorithm is the circumvention of these problems.

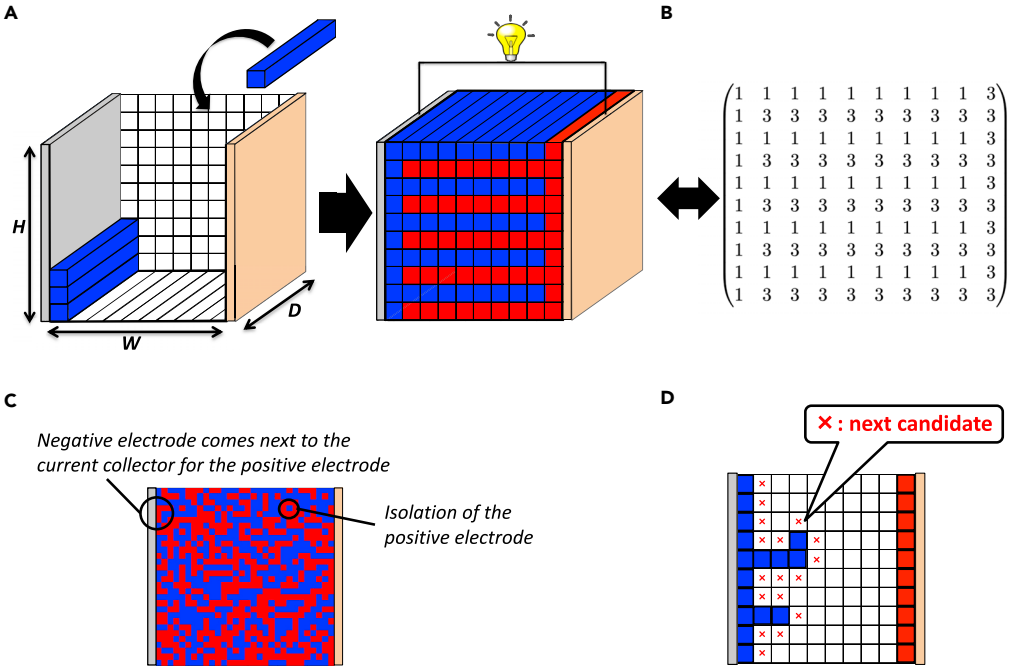

Figure 2. The Battery Generation Method

(A) The central idea of the battery generation. The battery cell is divided into finite elements, and the divided space is filled in with the electrode elements.

(B) The matrix to represent the battery geometry shown in (A), where "1" and "3" represent the positive and negative electrode elements, respectively.

(C) One example of the battery geometry generated by the random sampling with no restrictions, and examples of problems as a battery. The battery cell is divided into 30 × 30 elements.

(D) A list of the possible positions for the next positive electrode element. Blue and red squares represent positive and negative electrode elements, respectively. For simplicity, the separator at the interface between two electrodes is neglected in the figures.

The detailed protocol to generate the geometry matrix is as follows:

1. The battery size ($W \times H \times D$), the thickness of the separator, the resolution of the finite element mesh, and the volume ratio of the positive and negative electrodes are specified in the input data.
2. The numbers of the positive and negative electrode elements are computed using the input data.
3. The geometry matrix (the vacant cell) is prepared.
4. All the elements in the first column of the geometry matrix are set to "1," and all the elements in the last column of the geometry matrix are set to "3."
5. The positions of the positive electrode elements are determined one by one, where a list of next candidate positions in the matrix is created each time a positive electrode element is placed, and the next location is picked up randomly from the list. The list is created to avoid the isolation of the electrodes and based on the rule that the positive electrode element can be placed only next to the existing positive electrode elements, but, if that causes the isolation of the vacant elements ("0s" in the matrix), such candidates are removed from the list (Figure 2D). The isolation (connectivity) of the vacant elements is checked using the breadth-first search algorithm (Cormen et al., 2009).
6. After placing all the positive electrode elements, all the "0s" in the geometry matrix are replaced by "3s," i.e., the negative electrode elements.

In step 4, the short circuit problem is avoided, and we avoid the isolation problem in step 5.

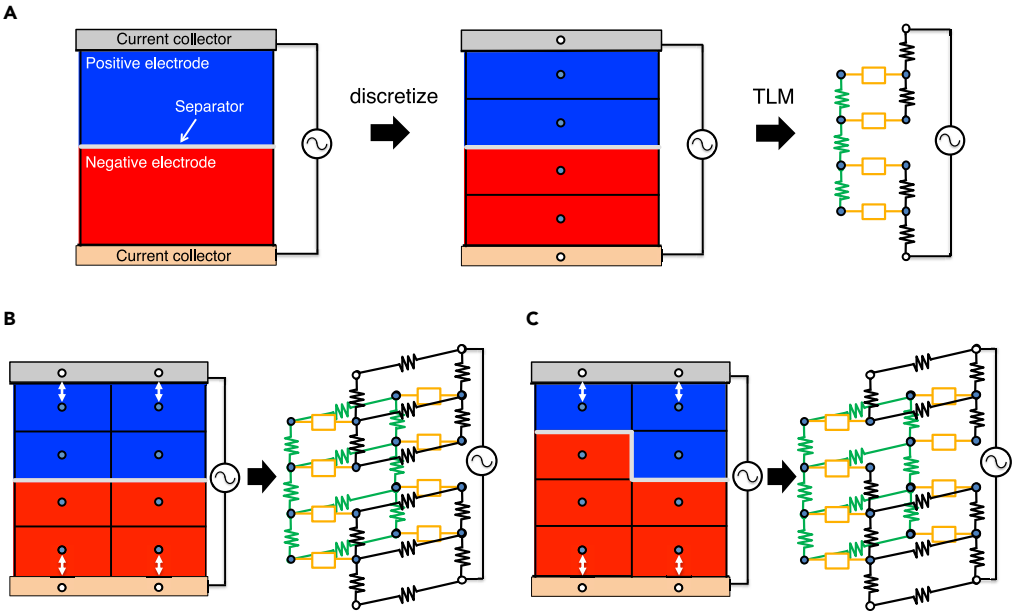

Figure 3. Comparison of the Conventional Transmission Line Model and the 3D Porous Electrode Model

(A) The conventional battery and the corresponding transmission line model when the system is divided into six elements including the current collectors.

(B and C) The 3D porous electrode model for the conventional battery (B) and the 3D battery (C) when the system is divided into six by two elements including the current collectors. The green- and black-colored resistances represent ionic and electronic resistances, respectively. The orange-colored rectangle represents the interfacial impedance and corresponds to the parallel circuit of the charge transfer resistance and the electric double-layer capacitance if the Faradaic process is assumed (Itagaki et al., 2007a).

Our geometry generation method is quite useful for the actual 3D battery design because the method can generate the geometry by following the required battery size and the resolution of the fabrication methods. Also, it is important to emphasize that we can evaluate the volumes of the electrodes and the separator directly from the geometry, which relate to the capacity of the battery.

The 3D Porous Electrode Model

One of our motivations in this article is to improve both the energy and power densities of the battery by changing the geometry of the electrodes, which corresponds to the reduction of the internal resistance (R_{inter}) while maintaining the capacity of the battery in this context. Although battery simulations using the continuum models are popular methods to evaluate R_{inter}, the methods are known to have a problem with their computational cost (McKelvey et al., 2020), especially when they are combined with the randomized algorithm because it generates a huge number of battery geometries, and R_{inter} values need to be evaluated for all. Therefore, in our approach, we evaluate R_{inter} using a computationally less-expensive equivalent circuit model.

As the lithium-ion battery generally uses the porous electrodes for both positive and negative electrodes, the equivalent circuit model has to describe the electrode reactions in the porous electrode to evaluate R_{inter} of the lithium-ion battery. The transmission line model (TLM) is known to be useful to capture such nature of the porous electrode (Itagaki et al., 2007a; Ogihara et al., 2012). The example of the TLM is illustrated in Figure 3A. As can be seen in the figure, TLM is constructed by the following three steps. At first, the battery cell is divided into some elements and, then, centers of the elements (which are represented by the circles in the figure) are connected by two kinds of resistances separately, i.e., ionic and electronic resistances. Finally, the two kinds of the series circuits (the series circuits of the ionic and electronic resistances) are connected by the interfacial impedances (the orange-colored rectangle). As both ion and electron paths exist inside the electrodes, the reactions inside the porous electrodes can be represented. When the TLM is used for electrochemical analyses of the conventional battery cells, the electronic resistance is often neglected and the analytical formula, i.e., the equation when the system is divided into infinite

number of elements, is used to investigate the cell impedance (Ogihara et al., 2012, 2015). It is noteworthy that, however, we do not use such an equation in our model, i.e., we construct the TLM from the finite number of elements.

We extend the TLM for use in three-dimensionally designed batteries, which we call the 3D porous electrode model. One of the key characteristics of the 3D porous electrode model is the introduction of one more degrees of freedom, as is clear from the comparison of Figures 3A and 3B. This allows representation of the geometrical difference of the electrodes, e.g., comparison of Figures 3B and 3C. The construction of the TLM is analogous to the conventional TLM. In our model, the electronic resistances in the current collectors are also considered in order for the stability of the calculations. The electronic resistance of the current collector is much smaller than other resistances, and, therefore, the influence of this treatment on R_{inter} is negligibly small. Here, we should note that the resolution of the 3D porous electrode model, i.e., the fineness of the finite element mesh, is not necessarily equal to that used for the battery generation, e.g., Figure 2A. To avoid any confusion, we call the element for the TLM as the TLM element. As mentioned previously, in this article, we allow 2D geometrical change to the electrodes, and, therefore, the corresponding TLM is for 2D design. However, it is straightforward to extend this model to the 3D batteries with the 3D designed electrodes.

The Electrical Resistance and Capacitance

To construct the 3D porous electrode model, the ionic and electronic resistances between the TLM elements and the charge transfer resistance in the TLM element have to be defined. Also, the electric double-layer capacitance (C_{dl}) in the TLM element is important to carry out the impedance analysis using our model. Ionic and electronic resistances (R_{ion} and R_{e}) between the same electrode elements (and the same current collector elements) are computed using the common equation given by

$$R\,[\Omega] = \rho\,[\Omega\mathrm{cm}] \times \frac{l\,[\mathrm{cm}]}{a\,[\mathrm{cm}^2]}\,, \qquad \text{(Equation 1)}$$

where ρ is the ionic or electronic resistivity and l and a are the length and cross-sectional area of the resistance that connects the centers of two TLM elements, respectively. Detailed definitions of ionic and electronic resistances (as well as the resistance between the electrode and the current collector) are given in the Transparent Methods section of the Supplemental Information.

The ionic resistance at the interface between the positive and negative electrodes is defined by

$$R_{\mathrm{ion}}^{\mathrm{pos/neg}} = \rho_{\mathrm{ion}}^{\mathrm{pos}} \times \frac{(l-s)/2}{a} + \rho_{\mathrm{ion}}^{\mathrm{neg}} \times \frac{(l-s)/2}{a} + \rho_{\mathrm{ion}}^{\mathrm{sep}} \times \frac{s}{a}\,, \qquad \text{(Equation 2)}$$

where s is the thickness of the separator and $\rho_{\mathrm{ion}}^{\mathrm{pos}}$, $\rho_{\mathrm{ion}}^{\mathrm{neg}}$, and $\rho_{\mathrm{ion}}^{\mathrm{sep}}$ are the ionic resistivities of the positive electrode, the negative electrode, and the separator, respectively. It is noteworthy that $\rho_{\mathrm{ion}}^{\mathrm{pos}}$, $\rho_{\mathrm{ion}}^{\mathrm{neg}}$, and $\rho_{\mathrm{ion}}^{\mathrm{sep}}$ are different from the ionic resistivity of the bulk electrolyte because it changes with the structural properties of the electrodes and the separator (e.g., the porosity of the separator). Also, we should note that we included the contributions of the positive electrode and negative electrode as well as that from the separator in $R_{\mathrm{ion}}^{\mathrm{pos/neg}}$ to remove the resolution dependence (the dependence of the fineness of the TLM element mesh) on R_{inter}. However, due to this treatment, only when $l = s$, $R_{\mathrm{ion}}^{\mathrm{pos/neg}}$ agrees with the electrolyte bulk resistance (R_{sol}) (Ogihara et al., 2012) and the simulated impedance spectrum can be compared with the experimental one.

The charge-transfer resistances of the positive and negative electrodes are defined by

$$R_{\mathrm{ct}}^{\mathrm{pos}} = \rho_{\mathrm{ct}}^{\mathrm{pos/sol}} \times \frac{1}{a_{\mathrm{reac}}^{\mathrm{pos/sol}}} \qquad \text{(Equation 3)}$$

$$R_{\mathrm{ct}}^{\mathrm{neg}} = \rho_{\mathrm{ct}}^{\mathrm{neg/sol}} \times \frac{1}{a_{\mathrm{reac}}^{\mathrm{neg/sol}}}\,, \qquad \text{(Equation 4)}$$

where ρ_{ct} and a_{reac} are the reaction resistivity ($\Omega\,\mathrm{cm}^2$) of the interface between the electrolyte and the active material in the electrode and the reaction surface area, respectively. In this article, the reaction surface area is assumed to be computed by

$$a_{\mathrm{reac}} = c v_{\mathrm{electrode}}\,, \qquad \text{(Equation 5)}$$

where $v_{electrode}$ is the volume of the electrode in one TLM element and c is the conversion factor. Although $v_{electrode}$ usually corresponds to the volume of the TLM element ($v_{element}$), $v_{electrode}$ is not equal to $v_{element}$ at the interface between the two electrodes due to the existence of the separator ($v_{separator}$) and is given by

$$v_{electrode} = v_{element} - v_{separator}. \quad \text{(Equation 6)}$$

By substituting Equation 5 into Equations 3 and 4, we obtain

$$R_{ct}^{pos} = \rho_{ct}^{pos/sol} \times \frac{1}{c^{pos/sol} v_{electrode}} = \frac{\sigma_{ct}^{pos/sol}}{v_{electrode}} \quad \text{(Equation 7)}$$

$$R_{ct}^{neg} = \rho_{ct}^{neg/sol} \times \frac{1}{c^{neg/sol} v_{electrode}} = \frac{\sigma_{ct}^{neg/sol}}{v_{electrode}}, \quad \text{(Equation 8)}$$

where we call $\sigma_{ct} (= \rho_{ct}/c)$ as the charge-transfer resistivity and the unit is $\Omega\ cm^3$.

The corresponding electric double-layer capacitances are defined by

$$C_{dl}^{pos}[F] = \epsilon_{dl}^{pos/sol}[F/cm] \times \frac{a_{reac}^{pos/sol}[cm^2]}{d_{dl}^{pos/sol}[cm]} \quad \text{(Equation 9)}$$

$$C_{dl}^{neg}[F] = \epsilon_{dl}^{neg/sol}[F/cm] \times \frac{a_{reac}^{neg/sol}[cm^2]}{d_{dl}^{neg/sol}[cm]} \quad \text{(Equation 10)}$$

where ϵ_{dl} and d_{dl} are the permittivity and the thickness of the electric double layer, respectively. By substituting Equation 5 into Equations 9 and 10, we arrive at

$$C_{dl}^{pos} = \epsilon_{dl}^{pos/sol} \times \frac{c^{pos/sol} v_{electrode}}{d_{dl}^{pos/sol}} = \zeta_{dl}^{pos/sol} v_{electrode} \quad \text{(Equation 11)}$$

$$C_{dl}^{neg} = \epsilon_{dl}^{neg/sol} \times \frac{c^{neg/sol} v_{electrode}}{d_{dl}^{neg/sol}} = \zeta_{dl}^{neg/sol} v_{electrode} \quad \text{(Equation 12)}$$

where the unit of the ζ_{dl} is F/cm^3. Here, we should note that the use of $v_{electrode}$ in Equations 7, 8, 11, and 12 removes the resolution dependence on the cell impedance from these terms.

Among the necessary parameters to compute the internal resistance or the cell impedance, the parameters related to the geometry, such as l, a, s, and $v_{electrode}$, are determined from the specifications of the battery and the resolution of the TLM. The other parameters are obtained from the AC (alternating current) impedance analysis of the symmetric cells (Ogihara et al., 2012, 2015; 2019; Itou et al., 2020). The necessary parameters to compute R_e and R_{ion} are the electronic and ionic resistivities (ρ_e and ρ_{ion}). σ_{ct} and ζ_{dl} have to be determined to compute R_{ct} and C_{dl}.

We determine σ_{ct} and ζ_{dl} from the AC impedance analysis of the symmetric cell. As the symmetric cell has two identical electrodes, the relationship between the experimentally measured charge-transfer resistance ($R_{ct}^{exptl.}$) and σ_{ct} is given by

$$R_{ct}^{exptl.} = \frac{\sigma_{ct}}{WD(H-s)/2} + \frac{\sigma_{ct}}{WD(H-s)/2} = \frac{4\sigma_{ct}}{WD(H-s)}, \quad \text{(Equation 13)}$$

where W, D, and H represent the width, depth, and height of the battery cell, respectively, and s represents the thickness of the separator. Here, we assume the separator is placed perpendicular to the height direction. Thus, σ_{ct} is obtained by

$$\sigma_{ct} = \frac{WD(H-s)}{4} R_{ct}^{exptl.}. \quad \text{(Equation 14)}$$

ζ_{dl} is determined using the relationship between the top of the capacitative semicircle (f_{max}) and the product of R_{ct} and C_{dl} that

$$R_{ct} C_{dl} = \frac{1}{2\pi f_{max}}. \quad \text{(Equation 15)}$$

By substituting Equations 7 and 11 (or Equations 8 and 12) into Equation 15, we obtain

$$\zeta_{dl} = \frac{1}{2\pi f_{max}\sigma_{ct}}. \quad \text{(Equation 16)}$$

Electrodes' Volume Effect on R_{inter}

In this article, we optimize the battery under the condition that the volume (V^{cell}) and shape of the battery cell are fixed and, therefore, the volume ratio between the separator (V^{sep}) and electrodes ($V^{electrode} = V^{cell} - V^{sep}$) changes with the electrode structures. The decrease of $V^{electrode}$ indicates the reduction of the total number of the lithium cation, leading to the increase of R_{inter}. As the 3D porous electrode model cannot describe this effect, we introduce this effect approximately using V^{cell} and $V^{electrode}$ as

$$R_{inter} = R_{inter}^{TLM} \times \frac{V^{cell}}{V^{electrode}}, \quad \text{(Equation 17)}$$

where R_{inter}^{TLM} denotes the internal resistance obtained using the 3D porous electrode model. We distinguish between R_{inter} and R_{inter}^{TLM} hereafter. It is noteworthy that although the charge-transfer resistance and the electric double-layer capacitance of the battery cell also change with $V^{electrode}$ because the reaction surface area (a_{reac}) changes, this effect is included in Equation 6.

Optimization of the Microbattery

We look for the 3D lithium-ion microbatteries that have both low internal resistance (R_{inter}) and high capacity by combining the automatic geometry generator and the 3D porous electrode model. Details of the computational conditions, including specification and resolution of the 3D lithium-ion microbattery and material property parameters, are given in the Transparent Methods section of the Supplemental Information (Figures S1–S3 and Table S1). Throughout this section, unless otherwise stated, we use the same resolution as the geometry generation for constructing the equivalent circuits, i.e., 50×10 TLM elements. Here, because the ρ_{ct} values are determined using the symmetric cells at the SOC (state of charge) of 50%, we simulate R_{inter} at this SOC. It is noteworthy that the battery performance at the SOC of 50% is considered to be important for practical applications. As for the capacity of the battery, as we design 3D electrodes under the constraint that the battery volume (V^{cell}) is constant and only the geometrical change of the electrodes is considered during the optimization, the ratio of electrode volume ($V^{electrode}$) to V^{cell} corresponds to the capacity of the battery. Thus, we evaluate $V^{electrode}/V^{cell}$ instead of the battery capacity. Also, even if constraints are introduced to the random geometry generation to produce only the acceptable geometries as the battery, still the search space is quite huge. Thus, we introduced the four kinds of periodicity conditions for the random geometry generations as shown in panel (A) of Figures S4–S7 in the Supplemental Information, where units of periodicity are 2 × 10, 5 × 10, 10 × 10, and 25× 10 elements, respectively. At each condition, we generate 50,000 geometries and evaluate $V^{electrode}$ and R_{inter} at each geometry. Even under such conditions, we can obtain complicated battery geometries beyond the interdigitated plates configuration as exemplified in Figure S7A.

All the R_{inter} data points (200,000 data points) are plotted as a function of $V^{electrode}/V^{cell}$ in Figure 4A. To understand the scaling effect introduced by Equation 17, R_{inter}^{TLM} data points are plotted in Figure 4B. For both figures, ideal batteries should come to the lower right edge. However, R_{inter} and $V^{electrode}$ has a trade-off relation, and, therefore, there are no such batteries. From the comparison of Figures 4A and 4B, the volume effect (Equation 17) influences the shape of the trade-off frontier at around $V^{electrode}/V^{cell} \leq 85\%$, when the thickness of the separator is 20 μm. However, in this region, the difference of the internal resistance on the trade-off frontier is small even in Figure 4A, i.e., the R_{inter} is in the range between around 60.0 and 70.0 Ω. This means that the volume effect is not so significant to design the 3D batteries at the current specification. However, this effect is important from the point of view of battery design for the developers.

We pick up four characteristic batteries as shown in Figure 4C. Geometry A is the conventional parallel plate configuration and shows the largest capacity ($V^{electrode}/V^{cell}$ = 96.7%), whereas it has the largest R_{inter} of 171.9 Ω. Although the geometrical difference between geometries A and B seems to be small, the drastic reduction of R_{inter} by 33.0 Ω is confirmed for geometry B. This indicates that even small modifications of the electrode structure strongly affect R_{inter}. Geometry C is the so-called interdigitated anode and cathode plates configuration and shows the smallest capacity ($V^{electrode}/V^{cell}$ = 71.1%) among all the generated geometries. However, indeed, this configuration is quite effective to reduce R_{inter} (= 69.1 Ω).

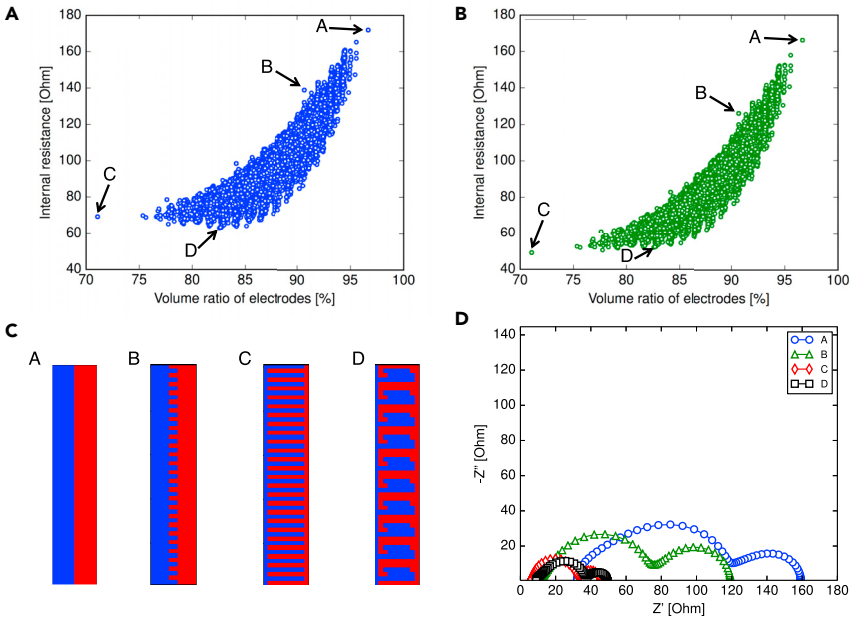

Figure 4. Results of Random Geometry Optimizations

(A) R_{inter} as a function of the volume ratio of electrodes ($V^{electrode}/V^{cell}$).

(B) R_{inter}^{TLM} as a function of the volume ratio of electrodes ($V^{electrode}/V^{cell}$).

(C) The characteristic geometries picked up from the results, where A–D correspond to A–D in panels (A) and (B).

(D) Nyquist plots of geometries A–D. To draw the Nyquist plots, the resolution of the 3D porous electrode model is set to be 150 × 30 elements. Also, the volume effect, which is shown in Equation 17, is not included.

Geometry D has the smallest R_{inter} (62.9 Ω) as well as good capacity ($V^{electrode}/V^{cell}$ = 82.6%), and we can expect that geometry D is superior to geometry C in terms of both energy and power densities.

From Figure 4A, there are a variety of geometries that have similar R_{inter} and $V^{electrode}$ in the low R_{inter} (e.g., R_{inter} of 60–70 Ω) and high $V^{electrode}$ (e.g., $V^{electrode}/V^{cell}$ of 80–85%) regions. This is an encouraging result from the point of view of the microbattery design because this implies that there is a space to improve other battery performances such as lifetime and thermal stability while maintaining good power and energy densities.

To clarify the 3D geometrical effect on R_{inter}^{TLM}, the Nyquist plots of geometries A, B, C, and D are compared in Figure 4D. In this analysis, we used 150 × 30 TLM elements to create the equivalent circuit. In this condition, l equals to s in Equation 2, meaning $R_{ion}^{pos/neg}$ agrees with the electrolyte bulk resistance (R_{sol}) (Ogihara et al., 2012). In this resolution, R_{inter}^{TLM} values slightly reduce to 159.23, 119.31, 45.29, and 49.31 Ω for geometries A, B, C, and D, and the corresponding R_{inter} values are 164.72, 131.58, 63.72, and 59.51 Ω, respectively. However, it is noteworthy that the order of the magnitudes of the R_{inter} values does not change regardless of the resolution of the transmission line model. Details of the resolution dependence are discussed in the following section. As the electronic resistance of the electrodes is small (Table S1 in the Supplemental Information), R_{inter}^{TLM} may be decomposed into five components as

$$R_{inter}^{TLM} = R_{sol}^{3D} + R_{ion}^{3Dpos} + R_{ct}^{3Dpos} + R_{ion}^{3Dneg} + R_{ct}^{3Dneg}, \quad \text{(Equation 18)}$$

where R_{ion}^{3Dpos} and R_{ion}^{3Dneg} represent contributions from the ionic resistance of the 3D positive and 3D negative electrodes and where R_{ct}^{3Dpos} and R_{ct}^{3Dneg} represent the charge transfer resistance of the positive and negative electrodes, respectively. Also, R_{sol}^{3D} denotes the electrolyte bulk resistance of the 3D battery. Here, we should note that R_{sol}^{3D} increases in proportion to the inverse of the interface area; R_{ion}^{3Dpos} and R_{ion}^{3Dneg} increase if the distance between the electrode element and the separator increase, which corresponds to the ion transport distance, and R_{ct}^{3Dpos} and R_{ct}^{3Dneg} reduce if the electrode volume increases.

For all the geometries, the Nyquist plots show two distorted semicircles. The semicircle at the lower Z′ region corresponds to the impedance of the negative electrode, and the width of the distorted semicircle

corresponds to $R_{ion}^{3Dneg} + R_{ct}^{3Dneg}$. The semicircle at the higher Z′ region corresponds to the impedance of the positive electrode. Also, the width between Z′ = 0 and the starting point of the semicircle of the negative electrode corresponds to R_{sol}^{3D}. As the width of the semicircle derived from the positive electrode of geometry A is almost the same as that of geometry B, the difference of the R_{inter}^{TLM} between geometries A and B comes from R_{sol}^{3D}, R_{ion}^{3Dneg}, and R_{ct}^{3Dneg}. Geometries C and D show much smaller semicircles as well as R_{sol}^{3D} than geometry A.

The main difference of R_{inter}^{TLM} between geometries C and D stems from the electrolyte bulk resistance (R_{sol}^{3D} of geometry C is 5.55 Ω and that of geometry D is 8.92 Ω). This is understandable by considering the fact that R_{sol}^{3D} increases with the inverse of the interface area between the two electrodes. Geometries C and D have similar electrode resistance (= $R_{ion}^{3Dpos} + R_{ct}^{3Dpos} + R_{ion}^{3Dneg} + R_{ct}^{3Dneg}$) because of the balance between the ionic and charge transfer resistances. Namely, geometry C has lower ionic resistance than geometry D because the number of electrode elements at the interface is higher, where the ion transport distance is the shortest. Contrary to this, geometry C has larger R_{ct}^{3Dpos} and R_{ct}^{3Dneg} because of the smaller electrode volume. Although geometry C has smaller R_{inter}^{TLM} than geometry D, R_{inter} of geometry D is smaller due to the volume effect (Equation 17). As a result, our method predicts that geometry D has better performance than geometry C by around 7% for R_{inter} and by 16% for the capacity.

We finalize this section by summarizing the advantages of our optimization system over the previously proposed 3D battery optimization methods based on the continuum model, where only simple structural change of the interdigitated electrodes is considered (Zadin et al., 2010, 2011; Zadin and Brandell, 2011; Priimägi et al., 2016; Miranda et al., 2016; Pikul et al., 2017). First, the use of the low-cost transmission line model allows R_{inter} evaluations of a variety of 3D battery geometries (e.g., 200,000 geometries), which is difficult with the continuum model. Here, we should emphasize that although the main benefit of the 3D electrode design is recognized to be the reduction of the ion transport distance (ionic resistance of the electrode) while maintaining the battery capacity (volume of the electrodes, which also relates to R_{ct}) (Pikul and Ning, 2018), the 3D porous electrode model can evaluate such effects. One of the main advantages of our geometry generator over the previously proposed methods is automatic battery design along with allowing much more flexibility in the electrode design. Also, in actual 3D battery design, the 3D battery has to be designed in a specified footprint area, e.g., Fu et al. (2016); Sun et al. (2013). In such a situation, the volume fraction of the electrodes and the separator changes with the electrode design. Our geometry generator takes into account such effect for the first time, whereas the previous works did not consider it. Therefore, our method is useful for the actual battery design. Effectiveness of the combination of the novel transmission line model and automatic geometry generator is demonstrated by finding new 3D battery architecture, which has better performance over the conventional interdigitated anode and cathode plates configuration.

Resolution Dependence of the 3D Porous Electrode Model

The internal resistance (R_{inter}^{TLM}) has the resolution dependence of the 3D porous electrode model. As shown in Figures 3B and 3C, the error in the internal resistance comes from three kinds of sources, i.e., the discretization of the system (the battery cell) into the finite number of TLM elements, the ionic resistances of the TLM elements next to the current collectors, and the electronic resistances of the TLM elements at the interface between two electrodes.

The first error source is intrinsic of our approach and the error comes from the approximation (discretization) of the system, which can be reduced by increasing the resolution (Itagaki et al., 2007b). As for the second problem, at the current implementation, the 3D porous electrode model does not compute the ionic resistances at the edge of the battery, which is shown as the white double arrows in Figures 3B and 3C. This error also can be reduced by improving the resolution of the 3D porous electrode model. Similar to the second problem, at the current implementation, our model does not compute the electronic resistance at the interface. However, it is noteworthy that this error is small because the contribution from the electronic resistance to the cell impedance itself is small as is clear from ρ_e values in Table S1 in the Supplemental Information.

In Table 1, we summarize the resolution dependence of the 3D porous electrode model on R_{inter}^{TLM} for geometries A–D in Figure 4C. As an overall trend, the order of the error is almost the same magnitude regardless of the geometry at the same resolution. Also, the size of the error is small even if the coarsest resolution (50 × 10 TLM elements) is used. Namely, the error is at most 7 Ω and the order of R_{inter}^{TLM}s among geometries A–D

Resolution	A	B	C	D
50 × 10	166.21 (6.98)	125.95 (6.64)	49.14 (3.84)	51.93 (2.80)
100 × 20	158.43 (− 0.80)	119.08 (− 0.23)	45.33 (0.04)	49.05 (− 0.08)
150 × 30	159.23 (0.00)	119.31 (0.00)	45.29 (0.00)	49.13 (0.00)

Table 1. Resolution Dependence on R_{inter}^{TLM} [Ω]
The error from the high-resolution result (150 × 30 TLM elements) is shown in parenthesis. A–D correspond to the geometries A–D in Figure 4C.

does not change. Although we further investigate the convergence of R_{inter}^{TLM} using higher resolution and thinner separator as shown in Table S2 in the Supplemental Information, the error from the coarsest resolution is small and decreases monotonically with the resolution. Therefore, we conclude that optimization using 50 × 10 TLM elements is reasonable and that the important conclusions that are drawn from Figure 4 do not change with the use of the finer resolutions, i.e., geometry D is superior to C in terms of power and energy densities and there is a possibility to improve other properties such as the lifetime while keeping high power and energy densities by changing the 3D geometry.

Conclusions

In this article, for the first time, we have proposed the battery optimization system at the full cell level, which consists of the automatic geometry generator and performance simulators. As geometry generator creates the battery automatically by only receiving the size and the resolution of the 3D battery cell, and volume ratio of the positive and negative electrodes as input data, any human intuition and experience are unnecessary for the spatial arrangement of the positive and negative electrodes. Also, as the resolution used in the generator can be set by following the resolution of the battery fabrication technologies, the direct design of the practical 3D battery is feasible.

As the battery design is a multiobjective optimization problem, quick performance evaluation methods are essential. As one of such methods, we proposed the 3D porous electrode model for the evaluation of the internal resistance of the 3D battery. The 3D porous electrode model can evaluate the internal resistance of the battery having 3D designed electrodes by simply introducing one more degree of freedom to the conventional transmission line model for the porous electrodes.

To demonstrate the effectiveness of our battery optimization system, we looked for the lithium-ion microbatteries that have both low internal resistance and high capacity. We created the trade-off frontier for the internal resistance and the capacity by generating 200,000 data points and successfully found that the 3D battery that has lower internal resistance and higher capacity over the conventional interdigitated battery. The new 3D battery showed better performance over the interdigitated geometry by around 7% for the internal resistance and 16% for the capacity. Also, we found that there were a variety of 3D batteries that have small internal resistance and high capacity. This is an encouraging result because this indicates that there is a possibility to improve other battery properties including cycle life and safeness, while maintaining good power and energy densities.

We strongly believe that our optimization system is compatible with 3D printing technologies. Especially, combination with direct ink writing (Fu et al., 2016; Sun et al., 2013) is expectable for the actual fabrication of the 3D battery.

As future work, we will improve the performance of the geometry generator by introducing sophisticated search algorithms such as Monte Carlo Tree Search methods and evolutionary algorithms (Browne et al., 2012; Wang and Sebag, 2013; Obayashi et al., 2007). Also, we will develop quick performance simulators for the other important battery properties, including thermal and mechanical properties as well as electrochemical properties.

Limitations of the Study

As our electrochemical model neglects ion diffusion and non-linear effects, influences of the lithium-ion depletion and the solid-state diffusion are not considered in the geometry optimization. Current in-house

python code can optimize only 3D batteries having two degrees of freedom for electrode design, and, therefore, extensions of both the geometry generator and the 3D porous electrode model are necessary for the full 3D battery design.

Resource Availability

Lead Contact

Further information and requests for resources should be directed to and will be fulfilled by the Lead Contact, Kaito Miyamoto (kaito.miyamoto@toyota.com).

Materials Availability

This study did not generate new materials.

Data and Code Availability

The dataset generated during this study (the battery geometries and associated electrode volumes and internal resistances) is available (https://doi.org/10.17632/c7zvggmh78.1).

METHODS

All methods can be found in the accompanying Transparent Methods supplemental file.

SUPPLEMENTAL INFORMATION

Supplemental Information can be found online at https://doi.org/10.1016/j.isci.2020.101317.

AUTHOR CONTRIBUTIONS

K.M., T.S., and K.T designed the transmission line model, and K.M., T.S., and T.N. designed the geometry generator. Y.I. conducted the experiment. K.M. developed the in-house python code and carried out the calculations. K.M. wrote the paper.

DECLARATION OF INTERESTS

Toyota Motor North America, Inc. has two patents pending related to this work.

Received: April 23, 2020
Revised: June 12, 2020
Accepted: June 24, 2020
Published: July 24, 2020

REFERENCES

Browne, C.B., Powley, E., Whitehouse, D., Lucas, S.M., Cowling, P.I., Rohlfshagen, P., Tavener, S., Perez, D., Samothrakis, S., and Colton, S. (2012). A survey of Monte Carlo tree search methods. IEEE Trans. Comput. Intell. AI Games *4*, 1–43.

Cormen, T.H., Leiserson, C.E., Rivest, R.L., and Stein, C. (2009). Introduction to Algorithms (MIT press).

Dudney, N.J. (2008). Thin film micro-batteries. Electrochem. Soc. Interf. *17*, 44.

Fu, K., Wang, Y., Yan, C., Yao, Y., Chen, Y., Dai, J., Lacey, S., Wang, Y., Wan, J., Li, T., et al. (2016). Graphene oxide-based electrode inks for 3D-printed lithium-ion batteries. Adv. Mater. *28*, 2587–2594.

Hart, R.W., White, H.S., Dunn, B., and Rolison, D.R. (2003). 3-D microbatteries. Electrochem. Commun. *5*, 120–123.

Hur, J.I., Smith, L.C., and Dunn, B. (2018). High areal energy density 3d lithium-ion microbatteries. Joule *2*, 1187–1201.

Itagaki, M., Suzuki, S., Shitanda, I., and Watanabe, K. (2007a). Electrochemical impedance and complex capacitance to interpret electrochemical capacitor. Electrochemistry *75*, 649–655.

Itagaki, M., Suzuki, S., Shitanda, I., Watanabe, K., and Nakazawa, H. (2007b). Impedance analysis on electric double layer capacitor with transmission line model. J. Power Sources *164*, 415–424.

Itou, Y., Ogihara, N., and Kawauchi, S. (2020). Role of conductive carbon in porous li-ion battery electrodes revealed by electrochemical impedance spectroscopy using a symmetric cell. J. Phys. Chem. C *124*, 5559–5564.

Izumi, A., Sanada, M., Furuichi, K., Teraki, K., Matsuda, T., Hiramatsu, K., Munakata, H., and Kanamura, K. (2012). Development of high capacity lithium-ion battery applying three-dimensionally patterned electrode. Electrochim. Acta *79*, 218–222.

Li, J., Liang, X., Panat, R., and Park, J. (2018). Enhanced battery performance through three-dimensional structured electrodes: experimental and modeling study. J. Electrochem. Soc. *165*, A3566–A3573.

Long, J.W., Dunn, B., Rolison, D.R., and White, H.S. (2004). Three-dimensional battery architectures. Chem. Rev. *104*, 4463–4492.

Markit, I.H.S. (2017). The internet of things: a movement, not a market. https://cdn.ihs.com/www/pdf/IoT_ebook.pdf.

Mazor, H., Golodnitsky, D., Burstein, L., Gladkich, A., and Peled, E. (2012). Electrophoretic deposition of lithium iron phosphate cathode for thin-film 3d-microbatteries. J. Power Sources *198*, 264–272.

McKelvey, K., Talin, A.A., Dunn, B., and White, H.S. (2017). Microscale 2.5 D batteries. J. Electrochem. Soc. *164*, A2500–A2503.

McKelvey, K., Cabré, M.B., and Paiva, A.E. (2020). Continuum simulations for microscale 3D batteries. Curr. Opin. Electrochem. *21*, 76–83.

Miranda, D., Costa, C., Almeida, A., and Lanceros-Méndez, S. (2016). Computer simulation evaluation of the geometrical parameters affecting the performance of two dimensional interdigitated batteries. J. Electroanal. Chem. *780*, 1–11.

Ning, H., Pikul, J.H., Zhang, R., Li, X., Xu, S., Wang, J., Rogers, J.A., King, W.P., and Braun, P.V. (2015). Holographic patterning of high-performance on-chip 3D lithium-ion microbatteries. Proc. Natl. Acad. Sci. U S A *112*, 6573–6578.

Obayashi, S., Jeong, S., Chiba, K., and Morino, H. (2007). Multi-objective design exploration and its application to regional-jet wing design. Trans. Jpn. Soc. Aero. Space Sci. *50*, 1–8.

Ogihara, N., Kawauchi, S., Okuda, C., Itou, Y., Takeuchi, Y., and Ukyo, Y. (2012). Theoretical and experimental analysis of porous electrodes for lithium-ion batteries by electrochemical impedance spectroscopy using a symmetric cell. J. Electrochem. Soc. *159*, A1034–A1039.

Ogihara, N., Itou, Y., Sasaki, T., and Takeuchi, Y. (2015). Impedance spectroscopy characterization of porous electrodes under different electrode thickness using a symmetric cell for high-performance lithium-ion batteries. J. Phys. Chem. C *119*, 4612–4619.

Ogihara, N., Itou, Y., and Kawauchi, S. (2019). Ion transport in porous electrodes obtained by impedance using a symmetric cell with predictable low-temperature battery performance. J. Phys. Chem. Lett. *10*, 5013–5018.

Pikul, J.H., and Ning, H. (2018). Powering the internet of things. Joule *2*, 1036–1038.

Pikul, J.H., Zhang, H.G., Cho, J., Braun, P.V., and King, W.P. (2013). High-power lithium ion microbatteries from interdigitated three-dimensional bicontinuous nanoporous electrodes. Nat. Commun. *4*, 1732.

Pikul, J.H., Braun, P.V., and King, W.P. (2017). Performance modeling and design of ultra-high power microbatteries. J. Electrochem. Soc. *164*, E3122–E3131.

Priimägi, P., Brandell, D., Srivastav, S., Aabloo, A., Kasemägi, H., and Zadin, V. (2016). Optimizing the design of 3D-pillar microbatteries using finite element modelling. Electrochim. Acta *209*, 138–148.

Sun, K., Wei, T.-S., Ahn, B.Y., Seo, J.Y., Dillon, S.J., and Lewis, J.A. (2013). 3d printing of interdigitated Li-Ion microbattery architectures. Adv. Mater. *25*, 4539–4543.

Swan, M. (2012). Sensor mania! the internet of things, wearable computing, objective metrics, and the quantified self 2.0. J. Sens. Actuator Netw. *1*, 217–253.

Wang, W., and Sebag, M. (2013). Hypervolume indicator and dominance reward based multi-objective monte-carlo tree search. Mach. Learn. *92*, 403–429.

Wei, M., Zhang, F., Wang, W., Alexandridis, P., Zhou, C., and Wu, G. (2017). 3D direct writing fabrication of electrodes for electrochemical storage devices. J. Power Sources *354*, 134–147.

Zadin, V., and Brandell, D. (2011). Modelling polymer electrolytes for 3D-microbatteries using finite element analysis. Electrochim. Acta *57*, 237–243.

Zadin, V., Kasemägi, H., Aabloo, A., and Brandell, D. (2010). Modelling electrode material utilization in the trench model 3D-microbattery by finite element analysis. J. Power Sources *195*, 6218–6224.

Zadin, V., Brandell, D., Kasemägi, H., Aabloo, A., and Thomas, J.O. (2011). Finite element modelling of ion transport in the electrolyte of a 3D-microbattery. Solid State Ionics *192*, 279–283.

Zadin, V., Brandell, D., Kasemägi, H., Lellep, J., and Aabloo, A. (2013). Designing the 3D-microbattery geometry using the level-set method. J. Power Sources *244*, 417–428.

Zhang, F., Wei, M., Viswanathan, V.V., Swart, B., Shao, Y., Wu, G., and Zhou, C. (2017). 3D printing technologies for electrochemical energy storage. Nano Energy *40*, 418–431.

Zhu, C., Liu, T., Qian, F., Chen, W., Chandrasekaran, S., Yao, B., Song, Y., Duoss, E.B., Kuntz, J.D., Spadaccini, C.M., et al. (2017). 3D printed functional nanomaterials for electrochemical energy storage. Nano Today *15*, 107–120.

iScience, Volume *23*

Supplemental Information

3D-Microbattery Architectural Design Optimization Using Automatic Geometry Generator and Transmission-Line Model

Kaito Miyamoto, Tsuyoshi Sasaki, Tomoki Nishi, Yuichi Itou, and Kensuke Takechi

Transparent Methods

Definition of the Ionic and Electronic Resistances

Electronic resistance ($R_{\mathbf{e}}$)

From Fig. 3, it is clear that there are six kinds of electronic resistances, i.e., the resistance between positive electrodes ($R_{\mathrm{e}}^{\mathrm{pos}}$), negative electrodes ($R_{\mathrm{e}}^{\mathrm{neg}}$), current collectors ($R_{\mathrm{e}}^{\mathrm{ccp}}$ for the current collector of positive electrode side and $R_{\mathrm{e}}^{\mathrm{ccn}}$ for negative electrode side), and that between the electrode and current collector ($R_{\mathrm{e}}^{\mathrm{pos/cc}}$ and $R_{\mathrm{e}}^{\mathrm{neg/cc}}$).

The resistance that connects the identical electrodes are defined by

$$R_{\mathrm{e}}^{\mathrm{pos}} = \rho_{\mathrm{e}}^{\mathrm{pos}} \times \frac{l}{a} \tag{1}$$

$$R_{\mathrm{e}}^{\mathrm{neg}} = \rho_{\mathrm{e}}^{\mathrm{neg}} \times \frac{l}{a} \, , \tag{2}$$

where $\rho_{\mathrm{e}}^{\mathrm{pos}}$ and $\rho_{\mathrm{e}}^{\mathrm{neg}}$ are the electronic resistivities of the positive and negative electrodes respectively, and where l and a are the distance and cross-sectional area of the resistance which connects the centers of two TLM elements.

The resistance between the current collectors are computed using similar equations as $R_{\mathrm{e}}^{\mathrm{pos}}$ and $R_{\mathrm{e}}^{\mathrm{neg}}$, i.e.,

$$R_{\mathrm{e}}^{\mathrm{ccp}} = \rho_{\mathrm{e}}^{\mathrm{ccp}} \times \frac{l}{a} \tag{3}$$

$$R_{\mathrm{e}}^{\mathrm{ccn}} = \rho_{\mathrm{e}}^{\mathrm{ccn}} \times \frac{l}{a} \, , \tag{4}$$

where $\rho_{\mathrm{e}}^{\mathrm{ccp}}$ and $\rho_{\mathrm{e}}^{\mathrm{ccn}}$ are the electronic resistivities of the current collectors for the positive and negative electrodes, respectively.

The resistance between the electrode and the current collector is defined by

$$R_{\mathrm{e}}^{\mathrm{pos/cc}} = \rho_{\mathrm{e}}^{\mathrm{pos}} \times \frac{l/2}{a} + \rho_{\mathrm{e}}^{\mathrm{ccp}} \times \frac{l_c}{a} \tag{5}$$

$$R_{\mathrm{e}}^{\mathrm{neg/cc}} = \rho_{\mathrm{e}}^{\mathrm{neg}} \times \frac{l/2}{a} + \rho_{\mathrm{e}}^{\mathrm{ccn}} \times \frac{l_c}{a} \, , \tag{6}$$

where l_c is the distance between the current collector and the edge of the electrode. Since $\rho_{\mathrm{e}}^{\mathrm{ccp}}$ and $\rho_{\mathrm{e}}^{\mathrm{ccn}}$ are nearly zero, $R_{\mathrm{e}}^{\mathrm{pos/cc}}$ and $R_{\mathrm{e}}^{\mathrm{neg/cc}}$ can be approximated as

$$R_{\mathrm{e}}^{\mathrm{pos/cc}} \approx \rho_{\mathrm{e}}^{\mathrm{pos}} \times \frac{l/2}{a} \tag{7}$$

$$R_{\mathrm{e}}^{\mathrm{neg/cc}} \approx \rho_{\mathrm{e}}^{\mathrm{neg}} \times \frac{l/2}{a} \, . \tag{8}$$

Ionic resistance ($R_{\mathbf{ion}}$)

Three kinds of ionic resistance are shown in Fig. 3, i.e., the resistance between the positive electrodes and the negative electrodes as well as that between positive and negative electrodes including the separator. The ionic resistances between the same electrodes are defined by

$$R_{\mathrm{ion}}^{\mathrm{pos}} = \rho_{\mathrm{ion}}^{\mathrm{pos}} \times \frac{l}{a} \tag{9}$$

$$R_{\mathrm{ion}}^{\mathrm{neg}} = \rho_{\mathrm{ion}}^{\mathrm{neg}} \times \frac{l}{a} \, , \tag{10}$$

where $\rho_{\text{ion}}^{\text{pos}}$ and $\rho_{\text{ion}}^{\text{neg}}$ are the ionic resistivities of the positive electrode and the negative electrode, respectively.

The ionic resistance at the interface between the positive and negative electrodes is defined by

$$R_{\text{ion}}^{\text{pos/neg}} = \rho_{\text{ion}}^{\text{pos}} \times \frac{(l-s)/2}{a} + \rho_{\text{ion}}^{\text{neg}} \times \frac{(l-s)/2}{a} + \rho_{\text{ion}}^{\text{sep}} \times \frac{s}{a} \,, \tag{11}$$

where s is the thickness of the separator and $\rho_{\text{ion}}^{\text{sep}}$ is the ionic resistivity of the separator. It is noteworthy that $\rho_{\text{ion}}^{\text{pos}}$, $\rho_{\text{ion}}^{\text{neg}}$, and $\rho_{\text{ion}}^{\text{sep}}$ are different from the ionic resistivity of the bulk electrolyte since it changes with the structural properties of the electrodes and separator.

Computational Details

We design the 3D lithium-ion microbatteries by allowing two-dimensional geometrical change of the electrodes. As shown in Fig. S1, the size of the battery cell is selected to be 3000 μm $\times$ 600 μm $\times$ 3000 μm excluding the current collector plates and the resolution of the electrode design is set to be 60 μm $\times$ 60 μm, meaning the battery cell is divided into 50 $\times$ 10 $\times$ 1 elements. The size and the resolution of the battery are determined based on the previous experimental studies, e.g., Sun et al. (2013) and Hur et al. (2018). Also, we set the volume ratio of the positive and negative electrodes as 1:1. The thickness of the separator is set to be 20 μm.

Experimental data to determine material property parameters are measured using the symmetric cells, except for the electronic resistivities of the current collectors. Details of the measurement methods are shown in Ogihara et al. (2012). Here, the mixture of $LiNi_{0.75}Co_{0.15}Al_{0.05}Mg_{0.05}O_2$, (Kondo et al., 2007) carbon black, and polyvinylidene fluoride (PVDF) at a weight ratio of 85:10:5 is used as a positive electrode; and the mixture of the graphite and PVDF at the weight ratio of 95:5 is used as the negative electrode. A microporous polypropylene film is used as the separator and, as a supporting electrolyte, 1.0 M $LiPF_6$ dissolved in a mixed solvent (which consists of ethylene carbonate, dimethyl carbonate, and ethyl methyl carbonate at the volume ratio of 3:4:3) is used. Aluminum and copper plates are chosen as the current collectors of the positive and negative electrodes respectively. The material property parameters are summarized in Table S1.

To investigate the validity of the materials property parameters and their determination methods that are described in the manuscript, the Nyquist plots obtained using the 3D porous electrode model are compared with the results of the AC impedance measurements using the symmetric cells, that are used to determine parameters in Table S1. As can be seen in Figs. S2 (b) and S3 (b) in the next section, the 3D porous electrode model well reproduces the Nyquist plots of the symmetric cells, meaning the parameters and their determination methods are valid.

All the calculations are performed using an in-house python code. The internal resistance and the impedance of the battery cell are computed using the node voltage method. Here, it is noteworthy that the interfacial impedance (the orange-colored rectangle in Fig. 3) becomes the charge-transfer resistance for the internal resistance calculations, and it becomes the parallel circuit of the charge-transfer resistance and the electric double-layer capacitance for the cell impedance calculations.

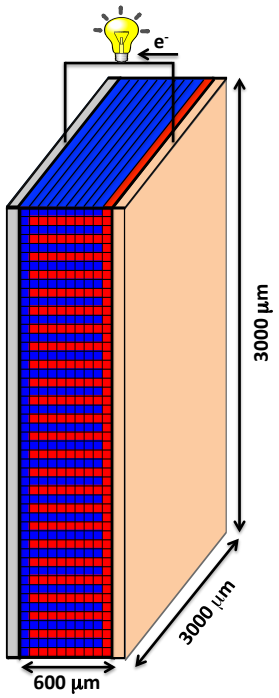

Figure S1: Specification and resolution of the 3D lithium-ion microbattery related to Figure 4 and Table 1. For simplicity, the separator at the interface between the two electrodes is neglected in the figure.

Table S1: Material property parameters used in the 3D porous electrode model related to Figure 4 and Table 1. It is noteworthy that $\rho_{\text{ion}}^{\text{sep}} = 1377.4$ [Ω cm] is used to optimize the 3D lithium-ion microbattery.

property	unit	positive electrode	negative electrode
electronic resistivity of the electrode (ρ_{e})	[Ω cm]	2.19	2.76
electronic resistivity of the current collector ($\rho_{\text{e}}^{\text{cc}}$)	[Ω cm]	2.632×10^{-6}	1.667×10^{-6}
ionic resistivity of the electrode (ρ_{ion})	[Ω cm]	857.1	1388.5
ionic resistivity of the separator ($\rho_{\text{ion}}^{\text{sep}}$)	[Ω cm]	1392.3	1377.4
charge transfer resistivity (σ_{ct})	[Ω cm^3]	1.663×10^{-2}	4.503×10^{-2}
double layer capacitance per unit volume (ζ_{dl})	[F cm^{-3}]	3.027	4.282×10^{-3}

Nyquist Plots of the Symmetric Cell

The Nyquist plot obtained using the 3D porous electrode model is compared with that from the symmetric cell using positive electrodes. Here, the state of charge (SOC) of the positive electrodes is set to be 50 %. The size of the symmetric cell is illustrated in Fig. S2 (a). As for the computational condition of the 3D porous electrode model, the size of the electrode is taken from the experimental condition given in Fig. S2 (a), but the thickness of the separator is set to be 2μm so that the finer grid can be used for the impedance computations. Then, the ionic resistance of the separator is revised by adding the correction factor given by

$$\Delta R_{\text{ion}}^{\text{sep}} = \rho_{\text{ion}}^{\text{sep}} \times \frac{s_2 - s_1}{W \times D} , \tag{12}$$

where $s_1 = 2\mu$m and $s_2 = 20\mu$m. In the 3D porous electrode model, the system is divided into 36 $\times$ 4 elements and the parameters in Table S1 are used for the simulation. The Nyquist plots obtained from the 3D porous electrode model and the AC impedance spectroscopy are compared in Fig. S2 (b). The Nyquist plot from the 3D porous electrode model well reproduces the experimental one.

The Nyquist plots of the symmetric cell using the two negative electrodes are compared in an analogous manner as that using positive electrodes. The size of the symmetric cell is illustrated in Fig. S3 (a). By setting the thickness of the separator to 2μm, the impedance values are computed using the 3D porous electrode model with the resolution of 86 $\times$ 4 elements. After correcting the ionic resistance of the separator using Eq. 12, the Nyquist plot is compared with that from the AC impedance spectroscopy as shown in Fig. S3 (b). Since the capacitative semi-circle from the AC impedance spectroscopy is distorted, the agreement is not so well compared with Fig. S2. But, still, the spectrum from the 3D porous electrode model well reproduces the experimental one.

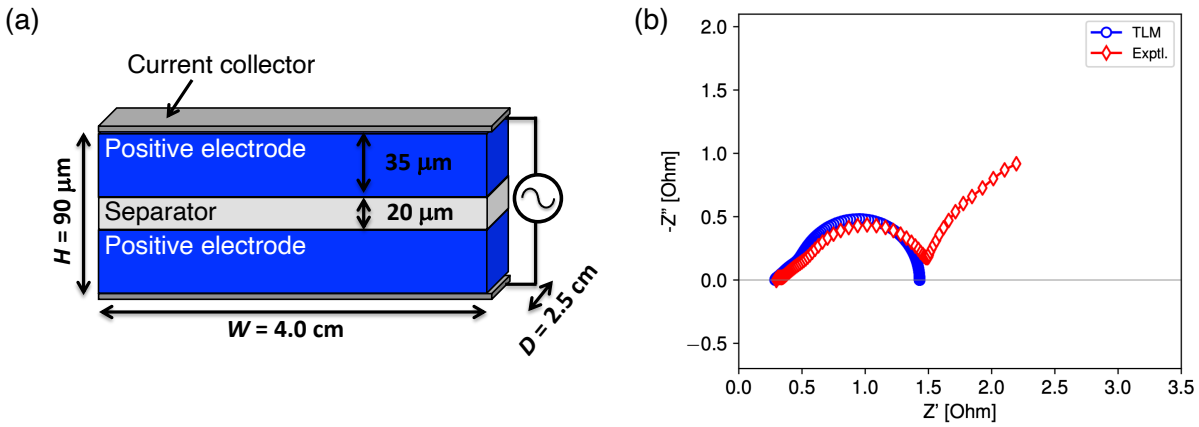

Figure S2: (a) Size of the symmetric cell using two positive electrodes. (b) Comparison of the Nyquist plots obtained from the 3D porous electrode model (TLM) and AC impedance analysis of the symmetric cell (Exptl.). $f_{\max}$ value from both the 3D porous electrode model and the AC impedance spectroscopy is 3.16 Hz. This figure is related to Figure 4 and Table 1.

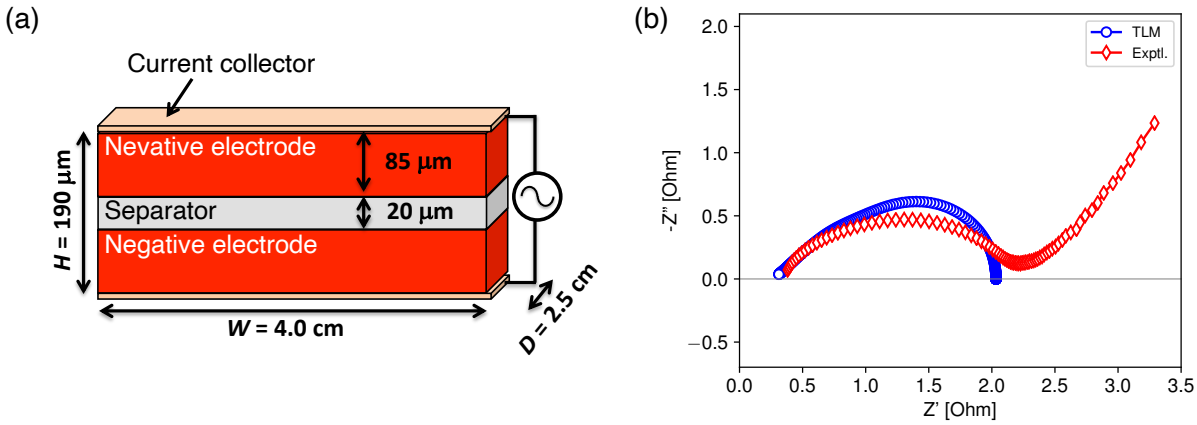

Figure S3: (a) Size of the symmetric cell using two negative electrodes. (b) Comparison of the Nyquist plots obtained from the 3D porous electrode model (TLM) and AC impedance analysis of the symmetric cell (Exptl.). $f_{\max}$ value from the 3D porous electrode model is 968.3 Hz, whereas that from the AC impedance spectroscopy is 825.4 Hz. This figure is related to Figure 4 and Table 1.

Results of Random Optimizations

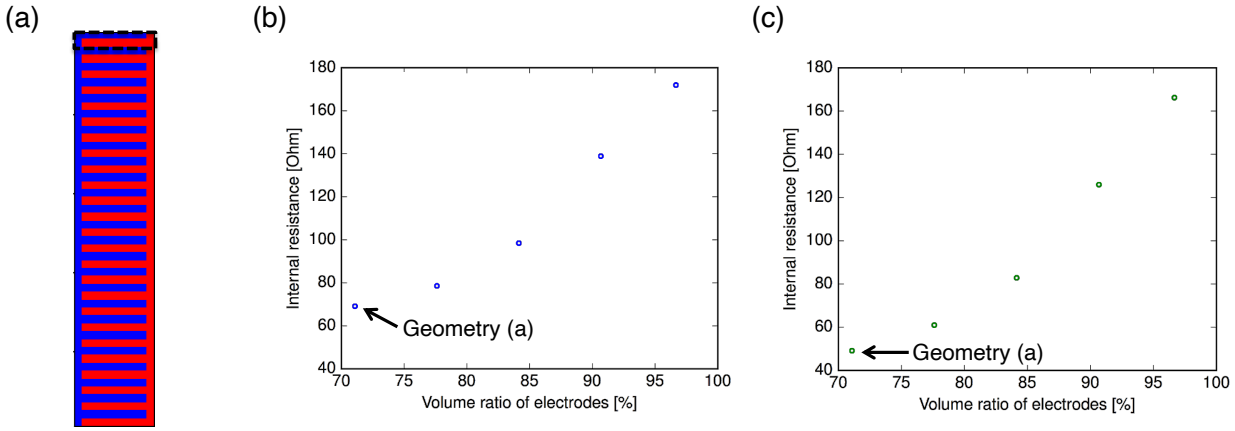

Figure S4: Results of random geometry optimization, where 50,000 data points are generated. (a) Unit of periodicity (2 × 10 elements: dotted square) and the geometry having the lowest R_{inter}. (b) R_{inter} as a function of the volume ratio of the electrodes. (c) $R_{\text{inter}}^{\text{TLM}}$ as a function of the volume ratio of the electrodes. This figure is related to Figure 4.

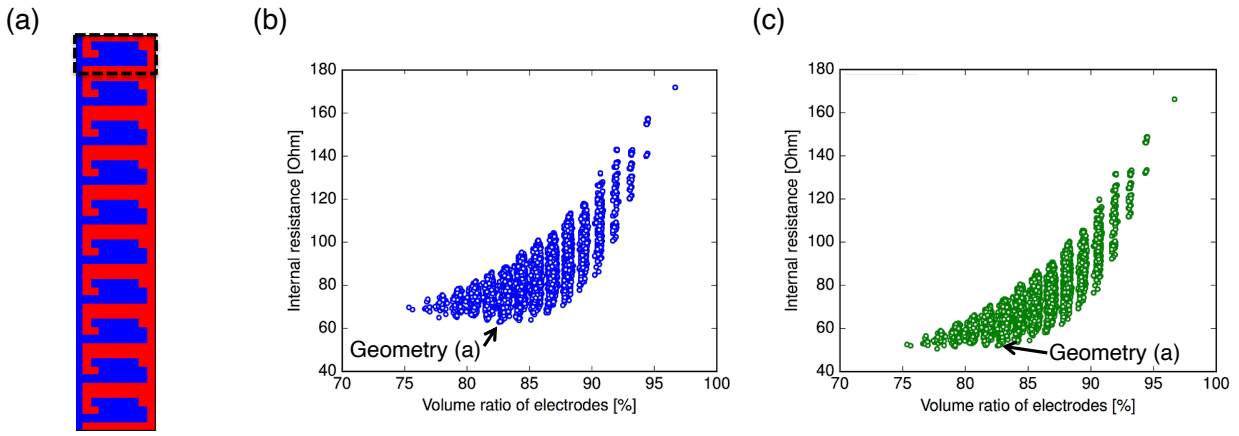

Figure S5: Results of random geometry optimization, where 50,000 data points are generated. (a) Unit of periodicity (5 × 10 elements: dotted square) and the geometry having the lowest R_{inter}. (b) R_{inter} as a function of the volume ratio of the electrodes. (c) $R_{\mathrm{inter}}^{\mathrm{TLM}}$ as a function of the volume ratio of the electrodes. This figure is related to Figure 4.

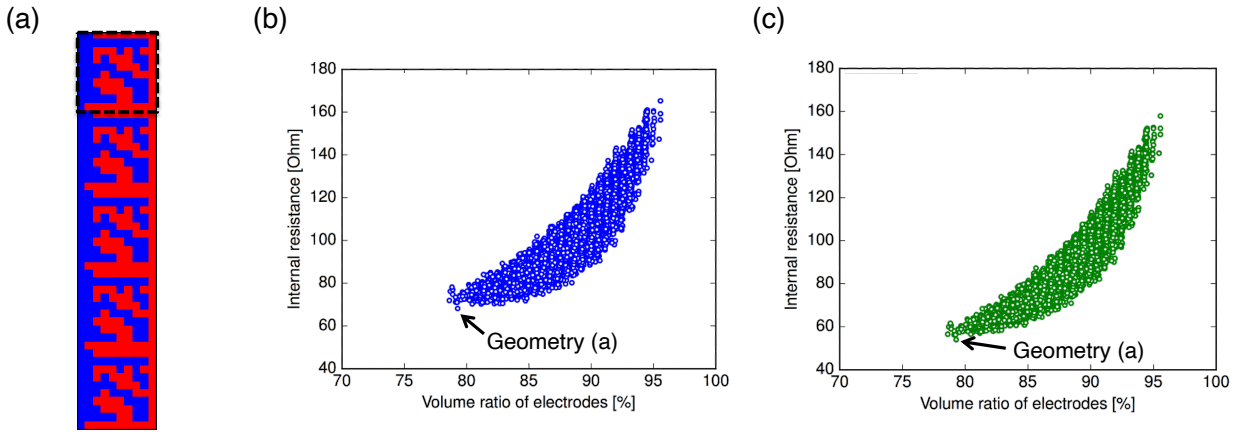

Figure S6: Results of random geometry optimization, where 50,000 data points are generated. (a) Unit of periodicity (10 × 10 elements: dotted square) and the geometry having the lowest R_{inter}. (b) R_{inter} as a function of the volume ratio of the electrodes. (c) $R_{\mathrm{inter}}^{\mathrm{TLM}}$ as a function of the volume ratio of the electrodes. This figure is related to Figure 4.

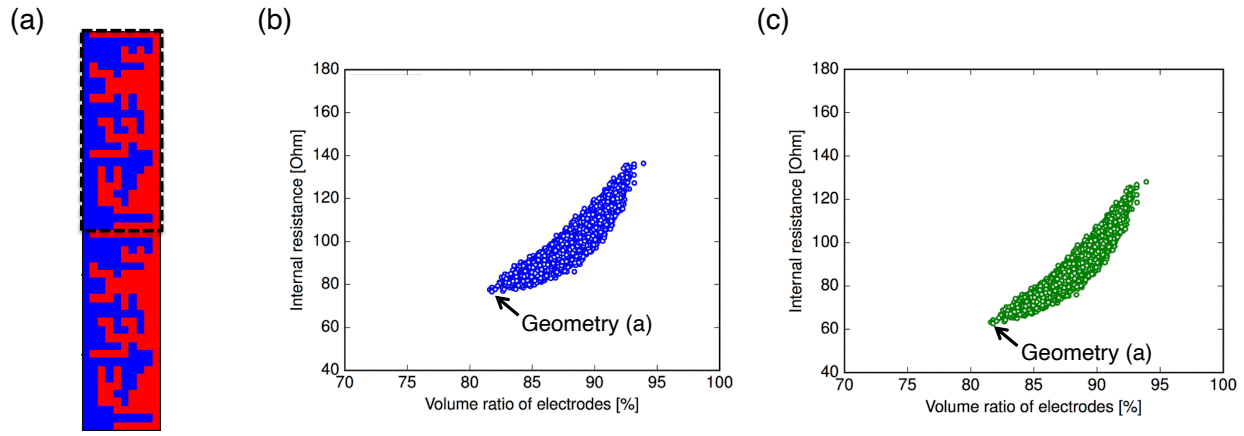

Figure S7: Results of random geometry optimization, where 50,000 data points are generated. (a) Unit of periodicity (25 × 10 elements: dotted square) and the geometry having the lowest R_{inter}. (b) R_{inter} as a function of the volume ratio of the electrodes. (c) $R_{\mathrm{inter}}^{\mathrm{TLM}}$ as a function of the volume ratio of the electrodes. This figure is related to Figure 4.

Numerical Assessment of the Resolution Dependence on the Internal Resistance using Thinner Separator

The resolution dependence of the 3D porous electrode model on $R_{\mathrm{inter}}^{\mathrm{TLM}}$ is investigated using thinner separator (2 μm) and the higher resolution than Table 1. Here, the thickness of the separator is changed in order to avoid the limitation of the current implementation of the 3D porous electrode model, i.e., the separator thickness has to be smaller than or equal to the one element size. We used geometry D in Fig. 4 (c) as the battery geometry. We confirmed that the error decreased monotonically and converged to 38.71 Ω, as shown in Table S2.

Table S2: Resolution dependence on $R_{\mathrm{inter}}^{\mathrm{TLM}}$ for geometry D in Fig. 4 (c) related to Table 1. The thickness of the separator is changed from the original value (20 μm) to 2 μm. The error from the highest resolution result is shown in parenthesis.

resolution	$R_{\mathrm{inter}}^{\mathrm{TLM}}$ [Ω]
50 × 10	44.48 (5.78)
100 × 20	40.12 (1.42)
150 × 30	39.28 (0.58)
200 × 40	38.99 (0.26)
250 × 50	38.87 (0.16)
300 × 60	38.80 (0.09)
350 × 70	38.76 (0.06)
400 × 80	38.74 (0.03)
450 × 90	38.73 (0.02)
500 × 100	38.72 (0.01)
550 × 110	38.71 (0.00)
600 × 120	38.71 (0.00)

References

Hur, J. I., Smith, L. C., and Dunn, B. (2018). High areal energy density 3d lithium-ion microbatteries. *Joule*, 2(6):1187–1201.

Kondo, H., Takeuchi, Y., Sasaki, T., Kawauchi, S., Itou, Y., Hiruta, O., Okuda, C., Yonemura, M., Kamiyama, T., and Ukyo, Y. (2007). Effects of Mg-substitution in Li (Ni, Co, Al) O2 positive electrode materials on the crystal structure and battery performance. *J. Power Sources*, 174(2):1131–1136.

Ogihara, N., Kawauchi, S., Okuda, C., Itou, Y., Takeuchi, Y., and Ukyo, Y. (2012). Theoretical and experimental analysis of porous electrodes for lithium-ion batteries by electrochemical impedance spectroscopy using a symmetric cell. *J. Electrochem. Soc.*, 159(7):A1034–A1039.

Sun, K., Wei, T.-S., Ahn, B. Y., Seo, J. Y., Dillon, S. J., and Lewis, J. A. (2013). 3d printing of interdigitated Li-Ion microbattery architectures. *Adv. Mater.*, 25(33):4539–4543.